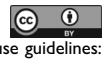
Check for updates

Special issue: MDA 2026

Institution of MECHANICAL ENGINEERS
Journal of MATERIALS: DESIGN AND APPLICATIONS

Proc IMechE Part L:
J Materials: Design and Applications
1–14
© IMechE 2026

Article reuse guidelines:
sagepub.com/journals-permissions
DOI: 10.1177/14644207261499555
journals.sagepub.com/home/pil


Predictive modeling of homogenized mechanical properties for multifunctional gyroid-based aerospace structures

Henri Kammler[1], Jan Kube[2], Hendrik Traub[2] and Christian Hühne[1,2]

Abstract

Gyroid sheet networks are a promising core structure for multifunctional sandwich panels, offering excellent load-bearing capabilities alongside omnidirectional permeability. The key to exploiting their full lightweight potential is to predict the homogenized mechanical properties based on readily available solid material parameters. This study develops material-independent predictive models for the homogenized compressive modulus, yield strength, and strength by separating the Gyroid's structural response from the contribution of the base material. Numerical and experimental investigations were carried out on Ti6Al4V and Nylon 11 at relative densities between 10% and 60%. Additional solid specimens form the basis for the material models and for normalizing the homogenized Gyroid properties. The results validate the material-independent modeling for the homogenized compressive modulus and yield strength across the entire investigated relative density range. The analysis of the homogenized compressive strength in combination with plastic strain distributions at the cellular level highlights the influence of base material strain hardening and ductility. Compared to the FE benchmark, practical imperfections reduce the experimentally measured homogenized mechanical properties by 15% to 35%. From an application perspective, the findings of this study establish a framework for designing load-bearing Gyroid cores for compressive stiffness and strength, independent of the specific base material.

Keywords

TPMS, Gyroid, lattice structure, suction panel, homogenized properties, material independent, predictive models

Received: 27 July 2026; accepted: 7 October 2026

Introduction

Gyroid sheet networks represent a promising core structure for additively manufactured lightweight structures. As part of the Triply Periodic Minimal Surface (TPMS) structures, their junction-free, self-supported geometry reduces local stress concentrations and enhances their resilience to stability failure, resulting in high material utilization and high weight-saving potential.[1,2] The open-cell architecture with its two interwoven internal channels not only allows the removal of resin or unsintered powder after Additive Manufacturing (AM) but also makes TPMS a favorable geometry for applications other than load-bearing structures. It enhances the chemical activity of catalysts,[3,4] promotes the regeneration of damaged tissue[5] and optimizes heat exchangers.[6]

Gyroid-based multifunctional core structures

Recent studies identify Gyroid sheet networks as a preferred core structure for multifunctional suction panels in aerospace applications.[1,7] Combining a micro-perforated surface[8] with an integrally manufactured permeable Gyroid core,[9] the panels effectively apply boundary layer suction on aircraft wings[10,11] and also transfer loads to the primary structure. Related studies investigate the mechanical behavior of the Gyroid structure under compression[12–14] and bending[15]- the two load cases that drive the design of suction panels. These studies distinguish between the inherent structural characteristics of Gyroid sheet networks and the influence of the base material by normalizing with the solid material properties. This enables comparability across different base materials and lays the foundation for predicting the homogenized material properties of TPMS structures.

Advanced design software such as *nTop* and *Altair inspire* facilitates the generation of cellular infill structures for complex parts to a great extent. Based on implicit formulations of the lattice in combination with spatial parameter variations, the cellular core structure can be optimized to meet a required compliance, minimize local stresses, and maximize material utilization. Design against failure, however, requires a subsequent computation to account for physical and geometrical nonlinearities. Especially for complex structures,

[1]German Aerospace Center (DLR), Institute of Lightweight Systems, Braunschweig, Germany
[2]Technische Universität Braunschweig, Institute of Mechanics and Adaptronics, Braunschweig, Germany

Corresponding author:
Henri Kammler, German Aerospace Center (DLR) Institute of Lightweight Systems, Lilienthalplatz 7, 38108, Braunschweig, Germany.
Email: henri.kammler@dlr.de

homogenizing the lattice infill and representing it as an effective material significantly reduces the computational cost.

Previous studies on mechanics of TPMS

The effective material properties of additively manufactured TPMS structures (denoted with *) are primarily influenced by three parameters: the mechanical properties of the 3D-printed solid base material (denoted with $_s$), the unit cell geometry, and the relative density RD that describes the volumetric fraction of the TPMS structure filled with the base material.[1] To facilitate the design and dimensioning of TPMS structures for mechanical applications, comprehensive models are required that predict the effective properties based on these fundamental parameters. This approach circumvents the need to simulate or manufacture and test the TPMS core structure of interest to derive its effective properties and enable its homogenization for the specific application. Motivated by the use case of multifunctional suction panels, this study focuses on the mechanical behavior of Gyroid sheet networks under quasi-static compression. It aims to distinguish between structural and base material effects to allow for material-invariant modeling.

The correlation between the base material properties P_s, relative density RD, unit cell geometry, and the effective mechanical properties of the TPMS structure P^* is often described empirically using a power law:[2] $P^* = P_s \cdot \alpha \cdot RD^n$. α and n, two dimensionless factors, are to be determined for the specific unit cell geometry. The theoretical upper limit is the Voigt limit $\alpha = n = 1$. It requires the base material to be free of imperfections and uniformly oriented along the load direction. It also neglects stability effects.[16] The study[2] provides an overview of numerical and experimental results on different TPMS structures. However, all values reported in[2] are based on absolute coefficients $C = P_s \cdot \alpha$. This representation obliterates the influences of the base material and structural mechanical effects and thus limits the comparability of the results.

Among the authors who mention their base material properties, many utilize the manufacturer's data sheet as the baseline, without any experimental validation.[17–19] This, however, is often error-prone, as the specific additive manufacturing process and environment significantly affect the material's mechanical behavior, resulting in deviations from the expected design values.[20] Other studies manufacture solid specimens and determine P_s experimentally, but under a different load case.[21–25] Only a few align with the best practice by manufacturing solid base material specimens utilizing identical process parameters and testing them under the same load case as their TPMS equivalents.[26,27]

Recent studies point out the value of representative relative parameters P^*/P_s.[12,13] Given that P_s and P^* are measured for the same load case, base material, and 3D printing parameters, P_s represents the upper limit of P^* for $RD \to 1$. In this case, P^*/P_s is a valid normalization and indicates the material utilization of the TPMS structure if divided by RD.[12]

Designing Gyroid sheet networks against failure based on literature results is further limited by inconsistent and partly arbitrary mechanical property definitions in the nonlinear deformation regime. The compressive strength in the literature is described using varied terminology (yield strength, fracture strength, specific compressive strength, etc.). Some studies use multiple terms, with no clarity on how the various terms differ from one another. However, the definitions can be broadly categorized into two sets: those defining the strength based on the first peak or maximum stress,[26–28] and those that utilize a parallel offset method, typically at 0.2% strain[29,30] or 1% strain.[19] Standards for the compressive properties of cellular plastics[31] and metallic materials[32] provide inconsistent definitions for the compressive yield point and strength.

Studies by Traub et al.[1,12] propose the investigation of material-invariant characteristics related to the Gyroid's mechanical behavior. They assume that the relative properties of Gyroid sheet networks are solely a function of the relative density $P^*/P_s = f(RD)$, given that the solid material properties P_s are representative for the solid phase of the cellular structure. In this case, the relative compressive modulus E^*/E_s and strength $\sigma^*_{max}/\sigma_{max,s}$ obey the polynomial scaling law derived by Gibson and Ashby[33] with the native points $P^*/P_s = 0$ at $RD = 0$ and $P^*/P_s = 1$ at $RD = 1$. Kammler et al.[13] validate the material-invariant characteristic $E^*/E_s = f(RD)$ of Gyroid sheet networks for a limited RD range by comparing their tested PA 11 specimens with literature results. They highlight the prerequisite of a stable, repeatable manufacturing process to ensure valid relative properties and a consistent criterion for compressive strength, to enable the validation of material-invariant parameters beyond the linear elastic regime.

This study addresses the research gap identified in the literature and extends the material-invariant characterization of Gyroid sheet networks to the compressive yield strength $R^*_{p,0.2}$ and compressive strength σ^*_{max}. Solid and cellular specimens ($RD = 10\%$, 20%, 40%) made of Ti6Al4V and Nylon 11 were tested under quasi-static compression to validate the predictive models for the Gyroid's stiffness and strength across different base material classes. Additional Finite Element Analyses (FEA), covering $10\% \leq RD \leq 60\%$, build upon the measured solid properties to provide a benchmark for assessing the experimental cellular properties and give insights into the non-uniform stresses at the cellular level. The results validate predictable material-independent characteristics of the relative compressive yield strength $R^*_{p,0.2}/R_{p,0.2,s}(RD)$ and the relative compressive strength $\sigma^*_{max}/R_{p,0.2,s}(RD)$ within the application-related relative density range for the investigated materials.

Experimental and numerical data acquisition

To establish material-independent correlations of the Gyroid's homogenized mechanical properties, quasi-static compression tests were performed experimentally and numerically between 10% and 60% relative density. The base materials Ti6Al4V and Nylon 11 were chosen as representative engineering materials for mechanically loaded additively manufactured components and to demonstrate the comparability of homogenized Gyroid properties through normalization across base material classes. This section

explains the design, specimen manufacturing, and testing along with the numerical data acquisition.

Specimen design

Cubic Gyroid specimens for compression tests were designed by defining their cellular parameters and main dimensions. The number of unit cells in each dimension n_{uc} determines the number of fully supported unit cells in the specimen center that scales with n_{uc}^3. The number of partially supported cells at specimen faces scales with n_{uc}^2. To ensure that the experimentally obtained results approximate the infinite lattice with a finite specimen size, the number of unit cells in each dimension should be $n_{uc} \geq 4$.[34] In this study, $n_{uc} = 4$ is used in all experimental and numerical tests.

The unit cell length l_{uc} and the thickness t of the symmetrically thickened minimal Gyroid surface determine the relative density RD according to:

$$RD \approx a \cdot \left(\frac{t}{l_{uc}}\right) + b \cdot \left(\frac{t}{l_{uc}}\right)^3 \quad (1)$$

with $a = 3.0918$, $b = -4.1887$, $R^2 = 0.99999$ for the Gyroid. The equation is based on the approach proposed by Traub et al.[12] Multiple Gyroid unit cells with varying wall thickness t were generated and their relative density RD was evaluated in Blender. Different regression approaches were compared, from which equation 1 was identified as a suitable analytical representation of the relative density as a function of t and l_{uc}. Kammler et al.[13] further visualize this relation and discuss typical combinations of parameters that are feasible for manufacturing.

The relative densities $RD = 10\%$, 20%, and 40% were investigated experimentally. The parameter l_{uc} was chosen based on a trade-off between reliable manufacturability, limited by the thinnest achievable wall thickness, and manufacturing costs. Furthermore, the capacity of available testing machines must be considered, as the maximum compressive forces scale with $A_{ref} = (n_{uc} \cdot l_{uc})^2$. In this study, l_{uc} is 16 mm for the Ti6Al4V specimens and 22.5 mm for Nylon 11 specimens. The resulting main dimensions (see Figure 1) are $l = w = h_G = 64$ mm for Ti6Al4V specimens and 90 mm for Nylon 11 specimens.

Specimens are designed using the software *Blender*. The implicit Gyroid equation f_G approximates the minimal surface for $f_G = 0$.

$$f_G = \sin X \cos Y + \sin Y \cos Z + \sin Z \cos X \quad (2)$$

with $X = 2\pi \cdot x/l_x$, $Y = 2\pi \cdot y/l_y$, $Z = 2\pi \cdot z/l_z$ at the Cartesian coordinates x, y, z with l_x, l_y, l_z being the unit cell length.[35] Equation 2 is evaluated for $f_G = 0$, and the Gyroid sheet network is obtained by thickening the isosurface by a constant t. The specimen faces are cut to the main dimensions $n_{uc} \cdot l_{uc}$ to ensure flat contact surfaces before STL files are exported.

Cylindrical solid specimens ($RD = 1$) were designed and manufactured to determine the compressive properties of the 3D-printed base material P_s. ASTM D695[36] for solid plastics defines long specimens (M, $d = 12.7$ mm, $h_M = 50.8$ mm) to determine the compressive modulus and short specimens (S, $d = 12.7$ mm, $h_S = 25.4$ mm) for the compressive strength.

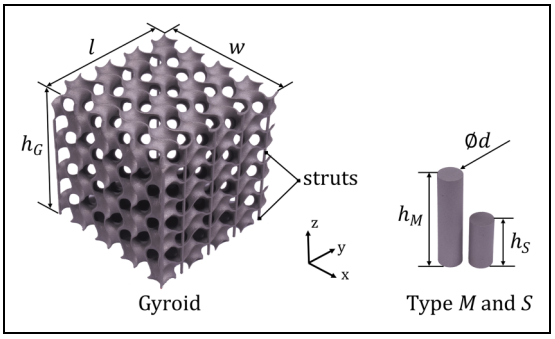


Figure 1. Main dimensions of an exemplifying Gyroid specimen (left) and solid specimens (right). h_G, h_M, and h_S denote the initial specimen heights, aligned with the printing and loading direction.

For type S specimens, DIN 50106[37] for solid metallic materials defines $1 \leq h/d \leq 2$, but does not address the investigation of the compressive modulus. In this study, ASTM D695 guides the design of Nylon 11 and Ti6Al4V solid specimens.

Additive manufacturing

The Ti6Al4V specimens were supplied by APWorks (Taufkirchen, Germany). At the vertical edges of the Gyroid specimens, support struts ensure manufacturability of overhanging cell portions (see Figure 1 left). The struts were removed manually before testing. A set of 5 specimens was manufactured for each relative density and for the solid specimen types S and M.

Nylon 11 specimens were manufactured using a Formlabs Fuse 1+ (30 W) SLS printer, Formlabs Nylon 11 powder, and a layer thickness of 0.11 mm. A nitrogen generator ensures an inert atmosphere in the build chamber with an oxygen concentration <0.2%. Unused powder was recycled with a refresh rate of 70%. After the printing process, the build chamber cooled down to room temperature before loose powder was removed from the specimens using brushes and thin rods. Finally, the specimens were sandblasted to remove powder that adhered to the surface. Two Gyroid specimens were manufactured using Nylon 11 for each relative density, rather than the five specimens originally intended. This reduced sample size was necessitated by manufacturing constraints and limits the statistical significance of the results. Five type S and M solid specimens complement the Nylon test series.

Solid specimens and Gyroid specimens were manufactured using the same printing parameters. Their printing direction (see Figure 1) aligned with the testing direction z. This method ensures the best agreement between the base material properties determined using the solid specimens and the material phase in the cellular specimens. Thus, the compressive stiffness E_s and compressive yield strength $R_{p\,0.2,s}$ of the solid specimens are considered the upper limit for the Gyroid specimens at $RD = 1$.

The main dimensions (see Figure 1) were measured for every specimen using a caliper to determine the reference area $A_{ref} = l \cdot w$ and $A_{ref} = d^2 \cdot \pi/4$ for the stress calculation and the initial height h for strain calculation. The mass of cellular specimens m^* and solid specimens m_s was determined using a precision scale to derive the densities ρ^*, ρ_s, and

Table 1. Main dimensions and relative densities of the specimens.

Material	Design	Measured RD	A_{ref}/mm^2	h/mm
Ti6Al4V	$RD = 0.1$	0.096 ± 0.001	4027 ± 4	64.7 ± 0.1
	$RD = 0.2$	0.192 ± 0.002	4015 ± 4	64.5 ± 0.1
	$RD = 0.4$	0.394 ± 0.001	4013 ± 7	64.4 ± 0.1
	Solid M	1	123.4 ± 0.5	51.2 ± 0.1
	Solid S	1	123.1 ± 0.5	25.8 ± 0.1
Nylon 11	$RD = 0.1$	0.094 ± 0.001	8105 ± 17	89.90 ± 0.4
	$RD = 0.2$	0.195 ± 0.001	8112 ± 1	90.1 ± 0.1
	$RD = 0.4$	0.397 ± 0.001	8115 ± 40	90.5 ± 0.1
	Solid M	1	127.0 ± 0.5	50.7 ± 0.1
	Solid S	1	127.7 ± 0.3	25.3 ± 0.3

the relative density $RD = \rho^*/\rho_s$. The analytical models presented in the results section refer to the measured relative density provided in Table 1.

Experimental compression tests

The Ti6Al4V specimens were tested under quasi-static compression using a hydraulic Zwick/Roell testing machine with a load capacity of 1 MN. A displacement transducer was attached to each compression platen to measure the displacement and determine the strain while accounting for machine compliance. The upper platen was fixed, while the lower platen moved along the z-axis. Force and displacement were recorded every 10^{-2} s. No additional measurement equipment was used for the cellular structures and the type S solid cylinders. To accurately determine the compressive modulus E_s of the solid Ti6Al4V, two strain gauges were attached to the type M specimens on opposite sides.

The testing speed for the Ti6Al4V Gyroid specimens was set according to DIN 50134[38] for compressive properties of cellular metallic structures. A strain rate of 10^{-3}/s corresponds to 3.84 mm/min, which is rounded to 4 mm/min. The testing speed was constant over the entire compression test. For the Ti6Al4V solid specimens S and M, the standards DIN 50106[37] and ASTM E9[32] apply. They specify strain rates of $25 \cdot 10^{-5}$/s and $8.3 \cdot 10^{-5}$/s, respectively. Considering the minimum speed of the machine (0.25 mm/min) and both mentioned standards, a testing speed of 0.5 mm/min was selected for both solid specimen types S and M.

The Nylon 11 specimens were tested on a 250 kN Zwick/Roell universal testing machine. The cross-head movement was used as a measure of deformation and strain. Force and displacement were recorded every 10^{-1} s or every $\Delta F = 1$ N, whatever occurred first. A calibration curve was recorded before testing and was applied automatically to the following tests. The strain rate for the cellular Nylon specimens was $1.6 \cdot 10^{-3}$/s according to[31,39] and corresponds to a speed of 9 mm/min. The testing speed of solid Nylon specimens was 1.3 mm/min according to.[36]

The cross-head was moved manually to apply a small preload (≈ 30 N for Nylon, ≈ 100 N for Ti6Al4V). The compression tests were conducted and stopped automatically if the machine limits specified above were reached or manually in case of complete failure. No data was recorded during unloading.

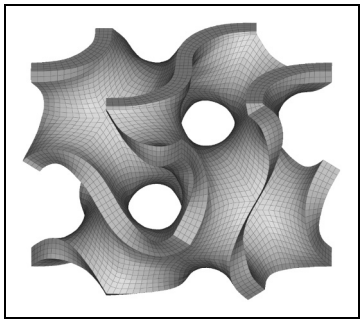


Figure 2. FE mesh illustrated by a single unit cell ($RD = 30\%$) at the top surface. $10 \cdot 10$ first-order elements for each of the 48 surface patches. 4 elements along the thickness. 2 additional element layers on the top ensure flat contact surfaces to compression platens.

Nonlinear FE model

The Finite Element Analyses performed in this study serve multiple purposes. On the one hand, they set a benchmark for the best possible homogenized Gyroid properties based on the measured solid material properties. This allows quantifying the overall experimental reductions, which include, among other effects, the influence of manufacturing imperfections. On the other hand, FEA provides the non-uniform stress distributions at the cellular level that help interpret the homogenized stress-strain responses in the context of the respective base material. Furthermore, the numerical models are used to investigate high relative densities that cannot be manufactured and tested.

Based on these considerations, the FE model used for this study consists of $4 \cdot 4 \cdot 4$ Gyroid unit cells, analogous to the experimental specimens. The Gyroid's minimal surface for $f_G = 0$ (Equation 2) was evaluated in Blender, exported as a fine STL mesh, and reconstructed in CATIA V5 using the auto surface option. In HyperMesh, each unit cell surface is split into 48 evenly sized rectangular patches that facilitate meshing with quadrilateral elements. Following the mesh convergence analysis described below, the minimal surface is meshed finely using $10 \cdot 10$ shell elements per patch, resulting in an element size of $\approx l_{uc} \cdot 0.03$.

Then, layers of fully integrated first-order hex elements (CHEXA8) were attached symmetrically to the shell elements on the minimal surface. The total sheet thickness was determined using Equation 1 and FE models were created for the relative densities $RD = 10\%$, 15%, 20%, 30%, 40%, and 60%. To minimize the effect of shear locking, four elements are aligned along the thickness t for $RD \leq 40\%$ and six elements for $RD = 60\%$.[40] Two additional element layers are used on the top and bottom of the FE Gyroid lattice to ensure flat contact surfaces, analogous to the experimental specimens. Figure 2 illustrates the mesh for a single unit cell ($RD = 30\%$) with two transition element layers on the top. The initially defined shell elements on the minimal surface were deleted before performing the analysis. In addition to the Gyroid geometry, rigid compression platens were defined to transfer the compressive load to the structure. The platens are discretized using CQUAD4 elements and coupled to an RBE2 reference node, which enforces rigid-body motion and effectively provides infinite

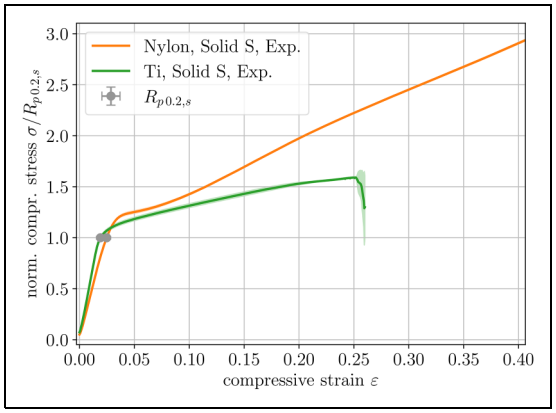


Figure 3. Normalized engineering compressive stress-strain graphs (averaged values and scatter bands) of solid specimens type S. Nylon solid specimens are tested up to ≈ 0.9 engineering strain without failure. Ti6Al4V specimens fail at ≈ 0.33 true strain.

stiffness. Frictionless contact is defined between the Gyroid structure and the compression platens. The lower platen is constrained in all degrees of freedom (DOF). The upper platen applies the compressive load through a displacement at constant velocity.

The experimentally determined compressive stress-strain curves of type S specimens (Figure 3) and compressive moduli E_s (type M, Table 2) define the MAT1 and MATS1 material cards. The linear-elastic regime is represented by E_s followed by the elasto-plastic behavior starting with $R_{p\,0.2,s}$. Before importing the curves into HyperMesh, engineering strains are converted to true strains using the equation $\varepsilon_{true} = |ln(1-\varepsilon_{eng})|$. True stresses are obtained using the equation $\sigma_{true} = |\sigma_{eng}(1-\varepsilon_{eng})^{2\nu}|$. Both equations take into account the positive sign of compressive stress and strain used in this work. The Poisson's ratio is approximated from literature values as $\nu = 0.323$ for Ti6Al4V[41] and $\nu = 0.4$ for Nylon.[42] The Poisson's ratio is considered constant. For Nylon 11 type S specimens, no distinct failure was observed until the experiments were terminated at a true strain of 1.6. The entire stress-strain curve is imported to define the MATS1 card. For Ti6Al4V, brittle failure is observed at an average true strain of ≈ 0.33 in the experiments with type S solid specimens (see Figure 3). Thus, failure is incorporated in the Ti6Al4V material model using a MATF card and enabling element deletion for equivalent true strains reaching 0.33. Progressive damage modeling is not employed, as the experiments for Ti6Al4V type S specimens show an abrupt failure and provide insufficient resolution to reliably characterize the damage evolution between damage initiation and final failure. To investigate the influence of fracture on the homogenized mechanical properties of the Gyroid lattice, additional analyses are performed for Ti6Al4V without considering the MATF card.

Nonlinear explicit analyses (NLEXPL) were performed using the OptiStruct solver. As this study focuses on the determination of the compressive strength, the analyses end after the first maximum in homogenized stress is reached. The plateau region and densification are not investigated in FEA. Internal contacts are not considered, since they do not occur for both materials and $RD < 0.6$ before the first stress maximum. The displacement was applied at a strain rate of 1/s. As no strain rate dependency is incorporated in the material definitions, the increased loading velocity compared to the experiments does not affect the material response. To reduce the computational cost of the explicit simulations, the material density is artificially increased by a factor of 100. For comparison, the Ti6Al4V configuration with $RD = 30\%$ was also analyzed without mass scaling, which confirmed the negligible influence of the artificially increased density on the mechanical response. The quasi-static nature of the simulations is confirmed by the kinetic energy remaining below 3% of the internal energy shortly after the onset of loading. The fully integrated CHEXA8 elements do not require artificial energy control. To suppress dynamic oscillations, the DYREL formulation available in OptiStruct was employed. Finally, the force and displacement at the top platen's single-point constraint (SPC) were exported to determine the homogenized stress-strain curves.

Table 2. Properties of solid materials Ti6Al4V and Nylon 11.

parameter	Ti6Al4V	Nylon 11
compr. modulus E_s	123 ± 2 GPa	1.76 ± 0.02 GPa
compr. yield strength $R_{p\,0.2,s}$	1150 ± 20 MPa	39.6 ± 0.5 MPa
compr. fracture strain	0.33 (true)	–
density ρ_s	4.338 g/cm^3	1.017 g/cm^3
Poisson's ratio ν	0.323[41]	0.4[42]

Calculation of material properties

The experimental and numerical data are analyzed in a common process. The homogenized compressive stress σ and compressive strain ε are calculated based on the initial reference area A_{ref} and the Gyroid specimen's initial height h_G: $\sigma = |F|/A_{ref}$ and $\varepsilon = |\Delta h|/h_G$. Both compressive stress and strain are defined to be positive in this study. The effective stress-strain values neglect inhomogeneous stress and strain distributions at the cellular level and consider the Gyroid structure as an effective material. In the same manner, compressive stress and strain are calculated for the solid specimens.

The compressive moduli of Gyroid specimens E^* and solid material E_s (using type M specimens) are obtained from the maximum slope during the initial rise in compressive stress. For this purpose, linear regression is carried out over successive strain intervals of $\Delta\varepsilon = 0.002$ (identical to the strain step in[43]). To account for the initial toe region in the stress–strain curve resulting from settling effects, the zero intercept of the elastic tangent is set as the new origin.

The compressive yield strength of the Gyroid $R^*_{p\,0.2}$ and solid material $R_{p\,0.2,s}$ (using type S specimens) is determined using the offset method. After calculating their compressive moduli and performing the toe compensation, the linear elastic tangent is shifted to 0.2% plastic strain. The intercept of the shifted linear elastic tangent with the specimen's stress-strain graph determines the compressive yield strength.

The compressive strength of the Gyroid specimens σ^*_{max} corresponds to the first local stress maximum $d\sigma/d\varepsilon = 0$ in the compressive stress-strain graph, irrespective of the

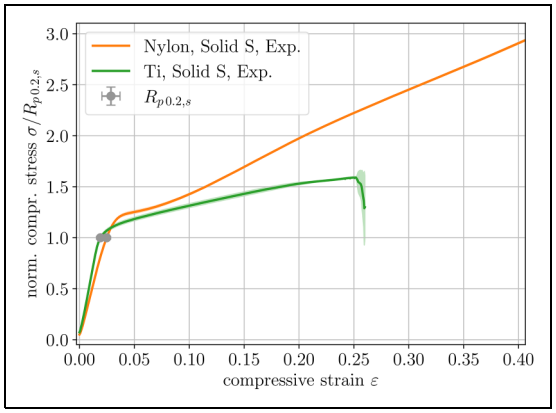


Figure 4. Mesh convergence analysis of a Gyroid unit cell with $RD = 30\%$. Homogenized properties $P^*_{uc,n}$ resulting from $n \cdot n \cdot 4$ elements per surface patch are plotted relative to the limit $P^*_{uc,\infty}$. The markers (•) represent sampling points, while the solid lines represent the fitted exponential curves.

arbitrarily defined 10% threshold in ASTM D1621[31] that is discussed in.[13] This decision ensures that the same strength criterion is applied to all Gyroid specimens tested and the shift of the compressive strength to higher strains with increasing RD is taken into account. The plateau region, energy absorption and densification are not investigated in this study. The compressive strength of the solid materials is not evaluated because the Nylon 11 type S specimens do not exhibit a distinct maximum or failure point in their stress–strain response (see Figure 3). To ensure comparability between the two base materials, the clearly defined compressive yield strength $R_{p,0.2,s}$ is therefore used as the sole measure of solid material strength.

Mesh convergence analysis

A mesh convergence analysis was performed for the Ti6Al4V configuration with $RD = 30\%$. To limit computational costs, a single unit cell was analyzed instead of the full $4 \cdot 4 \cdot 4$ lattice. Given the periodicity of the Gyroid structure, the mesh density identified for the unit cell is assumed to be transferable to the larger lattice. Each of the 48 surface patches was meshed with $n \cdot n \cdot 4$ hex elements (CHEXA8) where $4 \leq n \leq 15$. The homogenized compressive modulus E^*, yield strength $R^*_{p\,0.2}$, and strength σ^*_{max} are evaluated through nonlinear explicit analyses, and exponential curves are fitted as functions of the mesh density. Figure 4 illustrates the mechanical properties of the unit cell at each mesh density $P^*_{uc,n}$ relative to the limit value $P^*_{uc,\infty}$. For $n \geq 10$, the exponential curves of all three mechanical properties deviate by less than 2% from the limit value. Thus, $n = 10$ is considered a good trade-off between computational cost and accuracy. This mesh density was chosen for all numerical analyses in this study.

Results

The homogenized compressive stress–strain curves of the tested Gyroid sheet networks yield the mechanical properties and validate the FEA against the experimental data. Absolute values for stiffness and strength are provided in Table 3.

Table 3. Experimental and numerical results: Absolute values (mean and standard deviation) of the Gyroid's homogenized compressive modulus E^*, yield strength $R^*_{p\,0.2}$, and strength σ^*_{max}.

Material & Method	RD_{Design}	E^*/MPa	$R^*_{p\,0.2}$/MPa	σ^*_{max}/MPa
Ti6Al4V, FEA	0.10	3217	35.89	40.00
	0.15	5235	57.82	73.52
	0.20	7522	80.46	109.0
	0.30	12610	131.6	186.7
	0.40	19270	194.5	284.0
	0.60	35990	346.7	515.7
Nylon 11, FEA	0.10	43.63	1.19	1.31
	0.15	71.83	2.10	2.62
	0.20	103.2	2.92	4.19
	0.30	176.4	4.92	7.67
	0.40	271.9	7.36	12.34
	0.60	513.5	12.84	–
Ti6Al4V, Exp.	0.10	2440 ± 40	30.4 ± 0.2	34.2 ± 0.8
	0.20	6090 ± 30	75.3 ± 0.6	93.5 ± 0.2
	0.40	15500 ± 200	191 ± 2	–
Nylon 11, Exp.	0.10	34.0 ± 0.5	0.79 ± 0.02	1.01 ± 0.03
	0.20	89.9 ± 0.9	2.11 ± 0.02	3.50 ± 0.02
	0.40	266 ± 1	6.07 ± 0.05	10.7 ± 0.1

Based on normalized stress distributions at the cellular level, the influence of the base material and its elasto-plastic behavior on the homogenized strength parameters is evaluated. Finally, predictive models for the Gyroid's compressive modulus and strength are defined as a function of RD.

Solid material properties

Figure 3 illustrates the experimentally obtained compressive stress-strain response of Nylon 11 and Ti6Al4V type S specimens. These measurements provide the basis for defining the elasto-plastic material for the FE models and the values used to normalize the cellular structure's properties. The stress values plotted in Figure 3 are normalized with the respective compressive yield strength $R_{p\,0.2,s}$. Both stress and strain are engineering values. Scatter bands in the graph, representing the standard deviation, are barely visible and indicate good repeatability of the tests. Table 2 summarizes the measured solid material properties.

The materials show significant differences in their plastic behavior. While Nylon 11 is compressed up to 0.9 engineering strain without failure, brittle failure is observed for all Ti6Al4V specimens at an average true strain of ≈ 0.33. As the Nylon specimens show no local stress maximum, compressive strength cannot be defined for this material. Thus, the compressive yield strength $R_{p\,0.2,s}$ is used for normalization. A further difference between the two materials is observed in strain hardening. In the range $\varepsilon(R_{p\,0.2,s}) \leq \varepsilon \leq 0.2$ the engineering compressive stress of Nylon 11 increases by $\approx 0.11 \cdot E_s$. For Ti6Al4V, the increase is $\approx 0.02 \cdot E_s$.

Elasto-plastic behavior of Gyroid sheet networks

Figures 5 and 6 show the engineering stress-strain curves of Gyroid sheet networks determined through the experiments and their corresponding FEA for both base materials. For Ti6Al4V and $RD = 40\%$, the experimental curve ends

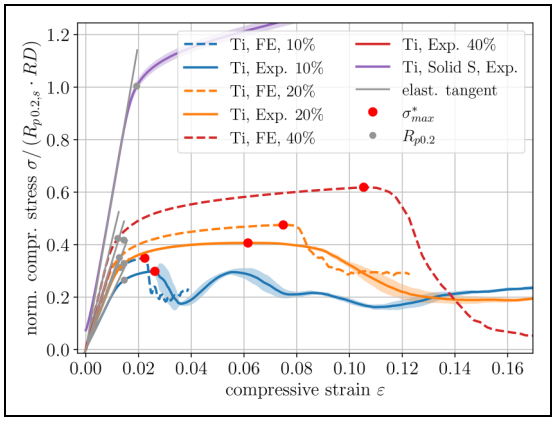


Figure 5. Ti6Al4V: Experimental and numerical engineering compressive stress-strain graphs (averaged values and scatter bands).

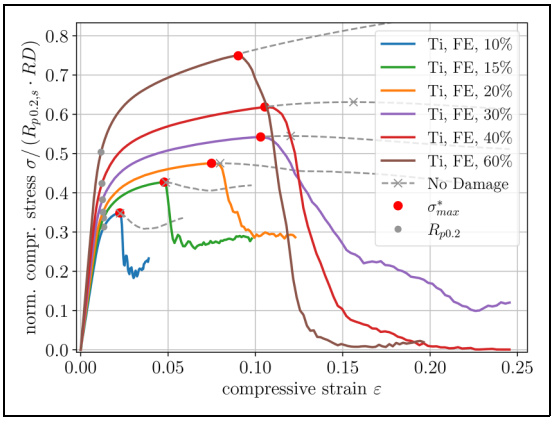


Figure 7. Ti6Al4V numerical results: Engineering compressive stress-strain graphs. RD ranging from 10% to 60%. Dashed *"No Damage"* progression obtained with ductile material model without element deletion.

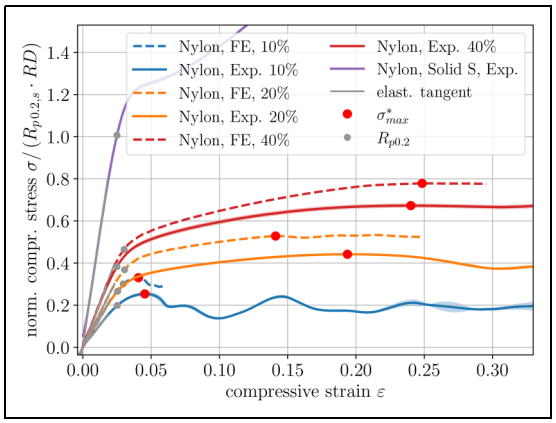


Figure 6. Nylon 11: Experimental and numerical engineering compressive stress-strain graphs (averaged values and scatter bands).

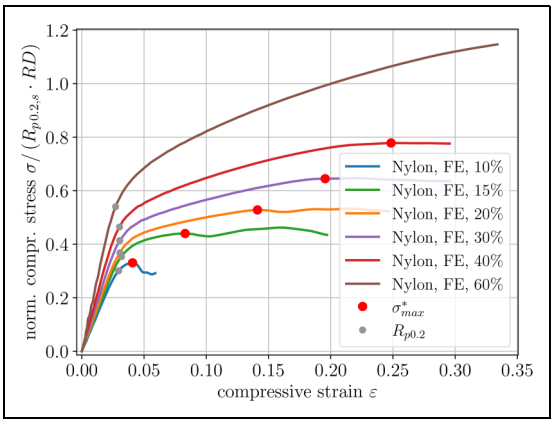


Figure 8. Nylon 11 numerical results: Engineering compressive stress-strain graphs. RD ranging from 10% to 60%. At $RD = 60\%$, no stress maximum is found before self-contact initiation.

within the elastic region due to the machine limits. To facilitate the comparability of different relative densities and base materials, the stress is normalized using the compressive yield strength of the corresponding base material $R_{p\,0.2,s}$ and the measured relative density RD. As $R_{p\,0.2,s} \cdot RD$ represents the theoretical upper limit for the yield strength of a cellular structure (Voigt maximum), this normalization allows an intuitive understanding of the specimen's mechanical efficiency.

Dashed lines represent the numerical results. They end shortly after reaching the first stress maximum, which marks the end of the investigated strain range in this study. Qualitatively, the FE results reflect the experimental curves very well. Quantitatively, the numerical method overestimates the experimental values by $15\% - 25\%$ in compressive modulus, compressive yield strength, and compressive strength.

For both base materials and methods, the normalized slope of the elastic tangent, compressive yield strength $R^*_{p\,0.2}$, and compressive strength σ^*_{max} increase with RD. Similarly, the compressive strength shifts towards higher strains. This shift causes a smoother transition from the elastic into the plastic plateau region. For Nylon 11, $\varepsilon(\sigma^*_{max})$ is about twice as high as for Ti6Al4V. The Ti6Al4V experiments and simulations show a distinct drop in compressive stress after reaching the compressive strength σ^*_{max}. This drop correlates with the initiation of cracks in highly loaded regions at the cellular level.

Additional relative densities $10\% \leq RD \leq 60\%$ are investigated using FEA. Figures 7 and 8 present all numerical analyses performed in this study. The additional numerical studies support the overall trends observed at $RD = 10\%$, 20%, and 40%. For Nylon 11 and $RD = 60\%$, no stress maximum is determined before the initiation of internal contacts, preventing the calculation of σ^*_{max}. The Ti6Al4V $RD = 60\%$ configuration exhibits another peculiarity. Here, the compressive strength followed by initiation of cracks occurs at a lower strain than for the $RD = 40\%$ geometry. This indicates a reversed trend in the intermediate RD range, with the ultimate strength and fracture occurring at $\varepsilon \approx 0.27$ at $RD = 1$ (see Figure 3).

Deformation and failure mechanisms

Figure 9a-d illustrates the typical deformation and failure behavior of Gyroid structures at low relative densities under

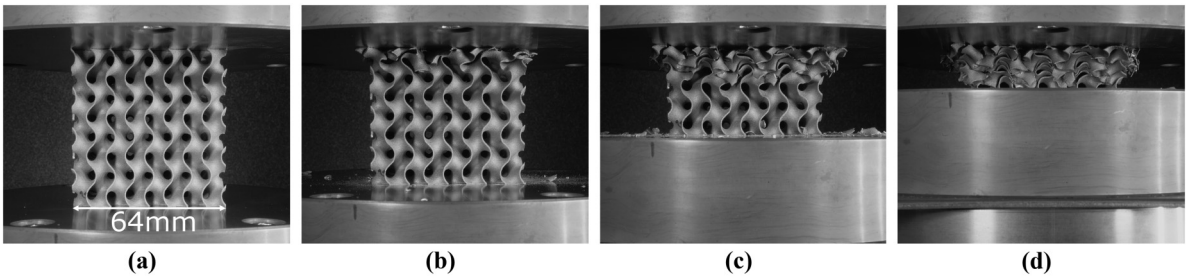


Figure 9. Gyroid specimen (Ti6Al4V, $RD = 0.1$, $n_{uc} = 4$) at $\varepsilon = 0.00$, 0.14, 0.45 and 0.67 engineering compressive strain.

quasi-static compressive loads. Stress and strain values for the depicted test are found in Figure 5 for $RD = 0.1$. A local maximum follows the linear elastic deformation and stress increase in the compressive stress-strain graph. Then, the collapse of the first cell layer is observed. While the first layer densifies, the collapse proceeds towards neighboring cell layers. In the corresponding plateau region, the compressive stress-strain graph undulates. Generally, no clear relation between local stress maxima and the collapse of cells can be observed as the collapse of individual cell layers progresses asynchronously. Once all layers are collapsed, the complete specimen densifies under steadily increasing stress. This observation also applies to Nylon 11 specimens with $RD = 10\%$.

In contrast to the horizontal layer-wise collapse, Ti6Al4V specimens at $RD = 20\%$ show diagonal, V-shaped or X-shaped cracks (Figure 10) along which the cells collapse and densify. The cracks appear after the first stress maximum is reached. Observed from the adjacent specimen face, this failure behavior can appear similar to the horizontal layer-wise collapse. For Ti6Al4V and $RD = 40\%$, no failure can be observed because the required force exceeds the machine's limits of 1 MN.

The FE analysis for Ti6Al4V at $RD = 10\%$ shows a qualitatively similar failure behavior to the experiments: The compressive strength σ^*_{max} is reached before a horizontal cell-layer starts to collapse. This collapse is initiated at the interface between the specimen and the compression platen. For Ti6Al4V $RD = 15\% - 20\%$ and Nylon $RD = 10\% - 30\%$, the FE models show a similar behavior. Here, the collapse of cells at the contact surfaces is superimposed by a slight shear deformation of the complete lattice. Only for Ti6Al4V at $RD = 30\% - 60\%$ do the FEA results show that material failure in the form of diagonal cracks causes an abrupt first maximum in stress identified as the compressive strength σ^*_{max}.

Stress distributions at the cellular level

The local stress and strain distributions at the cellular level provide the basis for assessing the influence of the elasto-plastic base material behavior on the Gyroid's compressive strength properties. Figures 11 and 12 demonstrate the von Mises stress distributions for both base materials and the relative densities $RD = 10\%$, 20%, 40% at the homogenized compressive yield strength $R^*_{p\,0.2}$ and homogenized compressive strength σ^*_{max}, respectively. The local stresses are normalized with the compressive yield strength of the solid base material $R_{p\,0.2,s}$ that marks the upper end of the color scale. Thus, the color red represents regions of yielding material.

The depicted unit cell is taken from the core cells of the simulated $4 \cdot 4 \cdot 4$ lattice to exclude effects of unsupported edges and stress concentrations at contact surfaces. For both base materials, methods, and every investigated RD, a homogeneous compression of the entire lattice free of cracks is observed at both stress levels, $R^*_{p\,0.2}$ and σ^*_{max}. The stress distributions point out highly loaded regions where the material is oriented along the loading axis.

The comparison between both base materials highlights almost identical relative stress distributions at $R^*_{p\,0.2}$ for the respective RD. With increasing RD, the yielding regions expand slightly, and the lowest stresses rise. Even though the base material starts to yield locally at a homogenized strain $\approx 10\%$ below $R^*_{p\,0.2}$, the maximum local plastic strain remains under 2% for both materials and the depicted RD. Thus, the base material's plastic behavior beyond $R_{p\,0.2,s}$ has little influence on the Gyroid's homogenized compressive yield strength $R^*_{p\,0.2}$. The quantitative analysis confirms this conclusion.

At the homogenized compressive strength σ^*_{max}, the relative stress distributions change significantly with increasing RD. For $RD = 10\%$ the relative stress distributions at σ^*_{max} and $R^*_{p\,0.2}$ largely agree for both base materials. For higher RD, regions of yielding material expand over large fractions of the unit cell, and differences between the two base materials become more apparent. Nylon 11 Gyroid specimens that exhibit first stress maxima at higher homogenized strains than Ti6Al4V yield almost completely at $RD = 40\%$ with local equivalent plastic strains reaching 63%. In contrast,

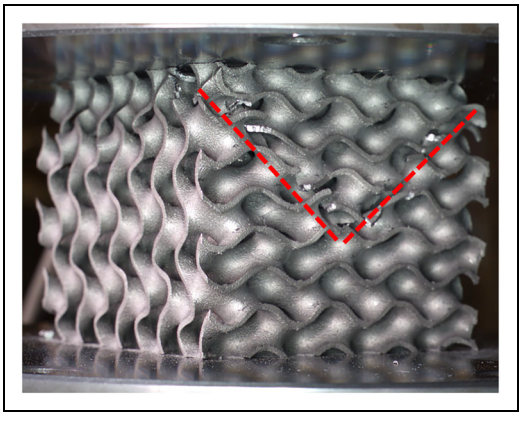


Figure 10. V-shaped cracks in a Ti6Al4V specimen ($RD = 20\%$) after exceeding the compressive strength.

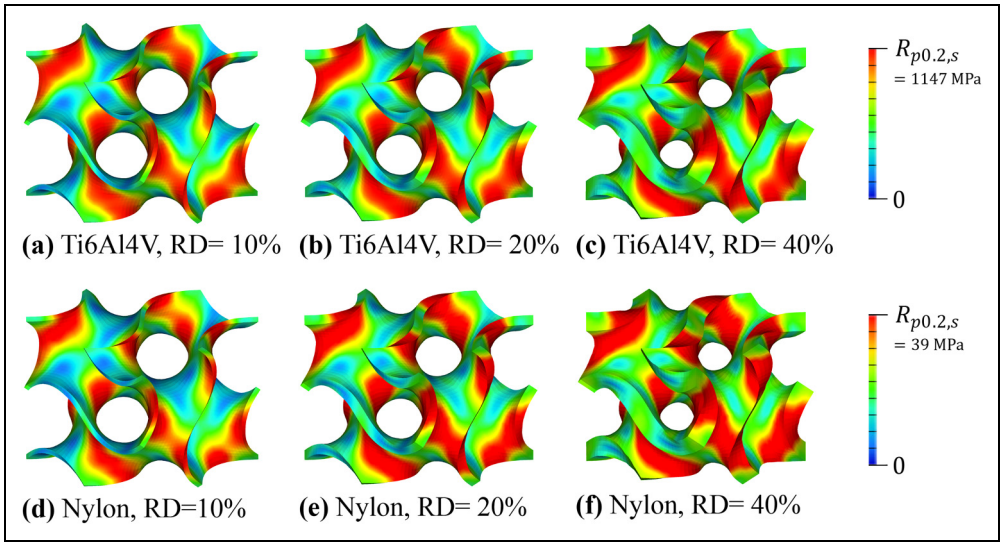


Figure 11. $R^*_{p\,0.2}$: von Mises stress distribution for an inner cell at the effective compressive yield strength of the Gyroid structure. Color scale adjusted to compressive yield strength of solid base materials $R_{p\,0.2,s}$.

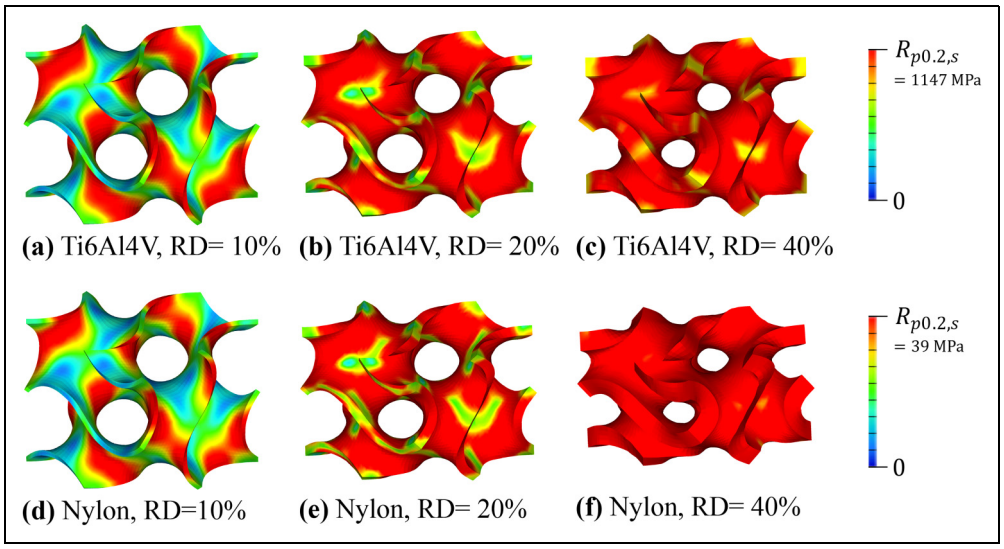


Figure 12. σ^*_{max}: von Mises stress distribution for an inner cell at the effective compressive strength of the Gyroid structure. Color scale adjusted to compressive yield strength of solid base materials $R_{p\,0.2,s}$.

local plasticity is limited to 33% true strain for Ti6Al4V due to failure. This results in σ^*_{max} being reached at a lower homogenized strain and leaves small fractions of the cell below the material's yield strength.

Additional FEA show that the material failure of Ti6Al4V mainly lowers the homogenized strain corresponding to the homogenized compressive strength σ^*_{max} at high RD. These analyses omit the MATF card and are represented by dashed gray lines in Figure 7. Below $RD \approx 20\%$ the limited ductility of Ti6Al4V does not influence σ^*_{max} significantly. At $RD = 20\%$, the first maximum occurs at a strain 0.5 percentage points ($\hat{=}6\%$) lower than in the analyses without damage. The effect on the corresponding stress (<0.1%) is negligible. For higher RD, the differences become more pronounced. At $RD = 40\%$, the first stress maximum, considering damage, occurs at a strain 33% lower than without. Due to the prolonged shape of the first stress peak, however, this corresponds to reduced σ^*_{max} of only 2%.

Mechanical potential as a function of the relative density

The good agreement between relative stress distributions at the cellular level of different base materials at the Gyroid's homogenized compressive yield strength underlines the aim to predict homogenized mechanical properties using material-independent models. This study investigates the normalized compressive modulus, yield strength, and strength as polynomial functions of RD. The results are presented in the order of increasing influence of plastic base material behavior.

Figure 13 presents the normalized compressive stiffness $E^*/(E_s \cdot RD)$ as a function of RD. Normalizing the relative modulus E^*/E_s by RD provides the mechanical potential in the linear-elastic region.[1] The experimentally obtained E_s marks the full mechanical potential for $RD = 1$ and is considered a native point for the modeling. Fourth-order

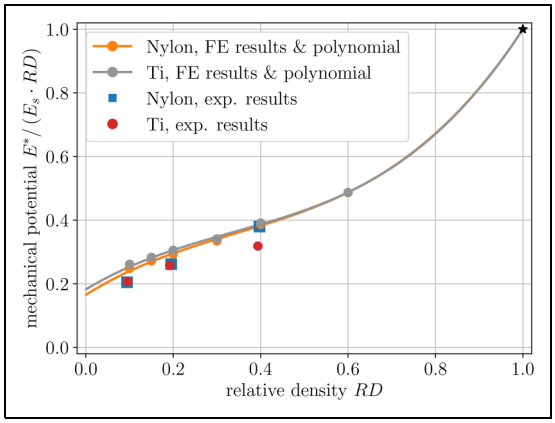


Figure 13. Mechanical potential of Gyroid sheet networks represented by the normalized compressive modulus $E^*/(E_s \cdot RD)$ and fitted over $RD = (0, 1]$ using polynomials. The asterisk represents a native point at $RD = 1$.

polynomials with the constant term equal to zero were selected for fitting the numerically determined E^*/E_s because they provide a close approximation of the available data points while maintaining a physically plausible response. The `curve_fit()` function provided by SciPy was used, which determines the polynomial coefficients by minimizing the sum of the squared residuals. The coefficients are provided in Table 4. The mechanical potential shown in Figure 13 is obtained by dividing the polynomials by RD. The standard deviation of experimental values is not visible in Figure 13 because it is lower than the width of the marker.

The mechanical potential of Gyroid sheet networks determined by FEA agrees very well for the base materials Nylon 11 and Ti6Al4V for all investigated RD. Differences between the base materials are below 4.8% and diminish with increasing RD. Thus, the numerical findings confirm the material-invariant approach for the mechanical potential $E^*/(E_s \cdot RD)$ across the two investigated base materials for $10\% \leq RD \leq 60\%$.

The fitted models follow an S-shape that predicts steadily increasing mechanical potentials for increasing RD. While the relative modulus E^*/E_s has a native point equal to zero at $RD = 0$, the mechanical potential $E^*/(E_s \cdot RD)$ approaches a non-zero value for $RD \to 0$ and is undefined at $RD = 0$ due to division by zero. As the models are based on data in the range $0.1 \leq RD \leq 0.6$, their predictive capability outside this range cannot be assessed. However, the mechanical potentials are known to attain a value of 1 at $RD = 1$, which provides a native point for the extrapolation.

The experimental tests at $RD = 10\%$ and 20% show good agreement in the mechanical potential of both base materials. For both RD, the scatter bands overlap, and the average values of Ti6Al4V and Nylon 11 specimens differ by less than 1.7%. Thus, the experimental results confirm the material-invariant mechanical potential of Gyroid sheet networks at $RD = 10\%$ and 20% for both investigated base materials. At $RD = 40\%$, Ti6Al4V yields a mechanical potential 16% lower than that of Nylon 11. To investigate this discrepancy, an additional FE study quantifies the influence of the platen compliance on the homogenized compressive modulus. The experimental platens were modeled using linear-elastic steel. For Ti6Al4V Gyroid specimens at $RD = 40\%$, E^* is reduced by 1.7% compared to the idealized rigid platens. Thus, the platen compliance has only a minor influence on the experimental results. The origin of the experimentally observed discrepancy remains unclear; however, manufacturing-related effects at high relative densities may contribute to the observed deviation.

In general, the experiments exhibit lower mechanical properties than the FE results. At $RD = 10\%$ and 20%, the numerically determined mechanical potential is $\approx 20\%$ higher than the experimental values. At $RD = 40\%$, it is 1.8% for Nylon 11. One possible explanation for this is the sensitivity of thin-walled structures to defects caused in the manufacturing process. The detailed characterization of manufacturing imperfections, however, is beyond the scope of this study. Instead, the experimental investigation focuses on evaluating the mechanical performance of Gyroid structures under application-relevant conditions. The observed reduction in mechanical properties relative to the idealized FEA results is consequently expressed in terms of general experimental reduction factors.

Predictive models for compressive strength

Figure 14 shows the numerical and experimental results regarding the homogenized compressive yield strength $R^*_{p\,0.2}$ and compressive strength σ^*_{max} for both base materials as a function of RD. In contrast to the mechanical potential $E^*/(E_s \cdot RD)$, the strength properties are normalized by the compressive yield strength of the corresponding base material and the relative density, resulting in $R^*_{p\,0.2}/(R_{p\,0.2,s} \cdot RD)$ and $\sigma^*_{max}/(R_{p\,0.2,s} \cdot RD)$. $R_{p\,0.2,s}$ provides a native point for the normalized compressive yield strength at $RD = 1$. The homogenized compressive strength σ^*_{max}, however, can exceed the base material's compressive yield strength $R_{p\,0.2,s}$ at high RD. Thus, no native point is defined for the normalized compressive strength at $RD = 1$. Fourth-order polynomials model the normalized strength properties. The coefficients are provided in Table 4.

In Figure 14, the numerical results of both base materials define envelopes for the normalized compressive strength properties. The normalized compressive yield strength (symbol $\triangledown$) reflects a minor influence of the two investigated base materials for $0.1 \leq RD \leq 0.6$. After the two curves intersect at $RD \approx 0.11$, they span a narrow region. At $RD = 0.6$, the normalized compressive yield strength of the Nylon 11 configuration exceeds that of the Ti6Al4V configuration by 7%. This difference is considered insignificant compared to the base materials' absolute compressive yield strengths $R_{p\,0.2,s}$ that differ by a factor of ≈ 29 (Table 2). Accordingly, Gyroid sheet networks made of the Ti6Al4V and Nylon 11 show a largely material-independent normalized compressive yield strength in the investigated relative density range. The experimentally determined values of Ti6Al4V specimens confirm the numerical results with 13% deviation at $RD = 10\%$ and less than 0.1% at $RD = 40\%$. Nylon 11 specimens exhibit a more pronounced deviation of $\approx 35\%$ at $RD = 20\%$ and 13% at $RD = 40\%$. In contrast to the numerically obtained envelope, the experimentally determined normalized compressive yield strength of Nylon 11 is considerably below that of Ti6Al4V for all investigated RD. It is assumed that the manufacturing of thin-walled

Table 4. Parameters to model relative properties according to $P^*/P_s = B \cdot RD + C \cdot RD^2 + D \cdot RD^3 + E \cdot RD^4$.

material and method	rel. property P^*/P_s	parameters				
		B	C	D	E	R^2
Ti6Al4V, FE	E^*/E_s	0.1824	0.8291	−1.3193	1.3079	0.9999
	$R^*_{p\,0.2}/R_{p\,0.2,s}$	0.2377	0.8142	−1.4652	1.4132	0.9999
	$\sigma^*_{max}/R_{p\,0.2,s}$	0.2353	1.4776	−1.8587	1.3716	0.9999
Nylon 11, FE	E^*/E_s	0.1654	0.8633	−1.3195	1.2908	0.9999
	$R^*_{p\,0.2}/R_{p\,0.2,s}$	0.2020	1.1920	−2.0226	1.6287	0.9999
	$\sigma^*_{max}/R_{p\,0.2,s}$	−0.0433	4.8974	−13.373	15.664	0.9999

Nylon 11 specimens using the described process introduces this reduction in homogenized compressive yield strength.

The normalized compressive strength $\sigma^*_{max}/(R_{p\,0.2,s} \cdot RD)$ determined by numerical analyses (symbol △) is represented by a wider range in Figure 14 and reflects a more significant influence of base material plasticity on the Gyroid's strength. At $RD \approx 13\%$, the Nylon 11 and Ti6Al4V curves intersect, causing minor differences <12% in the normalized compressive strength for both base materials between $RD = 10\%$ and 20%. With increasing RD, the Nylon 11 configuration exceeds the Ti6Al4V curve and ends 26% above it at $RD = 40\%$. This is the highest RD analyzed for which the numerical analysis for Nylon 11 exhibits a local stress maximum. At $RD = 60\%$ (x-marker), internal contacts are initiated before a stress maximum is observed. Thus, the Nylon 11 curve and the corresponding envelope end at $RD = 40\%$. The experimental results for the normalized compressive strength also reflect the intersection for both base materials between $RD = 10\%$ and 20%, while being ≈ 15% below the corresponding FE results. Accordingly, the reduction in compressive strength is less pronounced than in compressive yield strength.

The envelopes quantitatively verify the findings from the cellular stress distribution. Across all investigated relative densities and both base materials, the influence of plasticity on the homogenized compressive yield strength is small. Thus, the material-dependent hardening in the plastic regime has little effect on the relative compressive yield strength $R^*_{p\,0.2}/R_{p\,0.2,s}$, and the corresponding envelope is narrow. The good agreement of stress distributions across both base materials and strength properties at $RD = 10\%$ (Figure 11a/d and 12a/d) is confirmed quantitatively, as all four points deviate from each other by a maximum of 16%. For higher RD, the hardening of the respective base material has a stronger influence on the homogenized compressive strength as plastic strains at the cellular level increase and differ significantly between the two base materials. Thus, the more ductile Nylon 11, with its higher hardening in the plastic region relative to E_s, causes a steeper increase in the Gyroid's normalized compressive strength than the Ti6Al4V configuration.

Discussion

Using numerical analyses, this study underlines the material-independent character of the Gyroid's homogenized relative compressive modulus E^*/E_s for the base materials Nylon 11 and Ti6Al4V between 10% and 60% relative density. It extends and consolidates previous work, which proposed the material-independent modeling approach[12] and provided initial evidence by comparing experimental results with literature data.[13] The numerical sampling points and a native point at 100% define polynomial models that cover the entire RD range. Due to the lack of sampling points for $RD < 0.1$ and $0.6 < RD < 1$, the predictive accuracy of the models cannot be assessed in these ranges.

The experimental results of Nylon 11 and Ti6Al4V specimens with $RD = 10\%$ and 20% confirm the close agreement of the material-normalized compressive moduli across the two base materials. However, the limited number of Nylon 11 Gyroid specimens restricts the statistical robustness of this agreement. Future studies should therefore consider expanding the experimental database to further substantiate the observed consistency.

Compared to the numerical analyses, the experiments exhibit a reduction in homogenized compressive stiffness of ≈ 20% at low relative densities. This overall reduction can in part be attributed to the idealized cellular structure assumed in the FEA, which neglects manufacturing imperfections, as well as to the exclusion of compliance effects in the displacement measurements. Even though the material-independence of the relative modulus is demonstrated based on only two different materials, it is assumed that the polynomial models are also applicable to other base materials. This is because E^* is determined as the initial slope of the stress-strain curve that is not influenced by material-dependent nonlinearities.

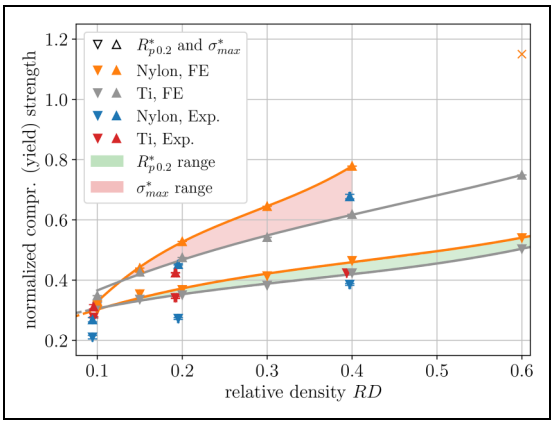


Figure 14. Normalized compressive yield strength $R^*_{p\,0.2}/(R_{p\,0.2,s} \cdot RD)$ and normalized compressive strength $\sigma^*_{max}/(R_{p\,0.2,s} \cdot RD)$ as a function of RD. Numerical and experimental results for Nylon 11 and Ti6Al4V. Envelopes visualize the influence of base material hardening.

The homogenized compressive yield strength $R^*_{p\,0.2}$ marks the end of the elastic deformation regime. Accordingly, $R^*_{p\,0.2}$ is determined at small deformations inducing minor geometrical nonlinearities. For relative densities $0.1 \leq RD \leq 0.6$, stresses at the cellular level exceed the base material's elasticity limit in relatively small highly loaded regions. Only here does the base material hardening contribute to the homogenized compressive yield strength. Due to low plastic strains at the cellular level, which are similar for both investigated base materials, $R_{p\,0.2,s}$ is a suitable value for normalizing the homogenized compressive yield strength $R^*_{p\,0.2}$. The remaining influence of base material hardening that is not reflected by $R_{p\,0.2,s}$ causes the polynomials of the FEA to span a narrow region as a function of RD. Thus, the models for compressive yield strength reflect an approximate material-independent characteristic for the base materials Ti6Al4V and Nylon 11 within the investigated relative density range. For lower relative densities (<0.1), the applicability of the results is unclear. It is expected that stability effects dominate the Gyroid's response to compression loads for low wall thicknesses t and cause premature failure. For relative densities beyond the investigated range ($RD > 0.6$), the native point $R^*_{p\,0.2}/R_{p\,0.2,s} = 1$ at $RD = 1$ provides a useful reference for estimating the compressive yield strength, although the exact relation remains uncertain.

Compared to the absolute compressive yield strength of both investigated base materials that differ by two orders of magnitude (Table 2), the deviations between the normalized numerical results are not considered relevant. Given that the base material is ductile enough to allow yielding of the Gyroid structure without initiating premature failure, it is expected that the models for the normalized compressive yield strength can also be applied to other base materials. Further studies are recommended to validate this claim using different engineering base materials. The maximum local plastic strain of 2% can serve as a reference value to evaluate the applicability of the normalized $R^*_{p\,0.2}$ models to more brittle base materials. Depending on the additive manufacturing process, base material, and other experimental influences, different reductions in compressive yield strength can occur that need to be subtracted from the FE-based models. This study suggests reductions between 13% and 35%.

Low plastic strains at the cellular level justify the normalization of the homogenized compressive yield strength by $R_{p\,0.2,s}$ for the entire RD range. For modeling the homogenized compressive strength σ^*_{max}, however, the material-independent normalization using $R_{p\,0.2,s}$ is limited to low relative densities around 10% to 20% that exhibit similarly low plastic strains at the cellular level. As $R_{p\,0.2,s}$ does not reflect the base material's hardening in the plastic regime, $\sigma^*_{max}/R_{p\,0.2,s}$ is significantly material dependent for high RD. This information is lost when comparing the relative stress distributions at the cellular level and truncating the color scale at $R_{p\,0.2,s}$ (see Figures 11 and 12). For Nylon 11 solid specimens and other potential base materials, no distinct compressive strength based on a stress peak can be determined that enables a more representative normalization of the Gyroid's homogenized compressive strength. Therefore, this study recommends the development of a novel compressive strength parameter generally applicable to stress-strain curves.

Even though the models of normalized compressive strength presented in Figure 14 are not unconditionally material-independent, they are considered to support designing Gyroid core structures against failure. It is assumed that sufficiently ductile materials with low strain hardening can be mapped to the lower end of the depicted envelope, while base materials with higher strain hardening correspond to the intermediate range or the upper end. The application-relevant relative density of $\approx 20\%$[9] for the proposed multifunctional suction panels falls within the validated range, which underlines the practical significance of the obtained results. At this RD, the normalized compressive strength is largely material-independent when comparing the described base materials with experimental reductions of $\approx 15\%$.

The predictive models for the homogenized mechanical properties developed in this study enable the systematic design of Gyroid core structures for compressive loading and the base materials Ti6Al4V and Nylon 11. Validation across a broader range of materials would unlock the full potential of the proposed models: Using only the base material properties as input, the analytical functions (Figures 13 and 14) allow the minimum relative density required to achieve a target homogenized stiffness and strength to be determined. Conversely, these analytical functions can be used to derive required base material properties for a prescribed relative density. This approach is particularly relevant when the relative density is constrained by design requirements associated with other functionalities of the core structure, such as permeability in the suction panel application considered here. For practical applications, it is recommended to use the analytical expressions obtained from the numerical models (Table 4) in combination with the experimentally determined knockdown factors corresponding to the respective mechanical property.

Conclusion and outlook

This study develops predictive models for the homogenized compressive stiffness and strength of Gyroid sheet networks to facilitate their mechanical design. The models are based on the assumption that the homogenized cellular properties P^* are determined by material-independent terms as a function of the relative density RD and scale linearly with the corresponding mechanical parameters of the solid base material P_s. Once its general applicability is validated, this modeling approach provides a significant advantage: The effort to predict the homogenized Gyroid properties for different materials is reduced to the experimental investigation of additively manufactured solid material specimens. Costly coupon tests or FEA of the Gyroid structure for the specific base material and relative density become obsolete.

To identify the predictive stiffness and strength models, the homogenized mechanical properties of Nylon 11 and Ti6Al4V were investigated using FEA and experimental quasi-static compression tests for relative densities between 10% and 60%. The numerical results validate the material-independence of the normalized compressive modulus, supported by the experimental results for both base materials within the given relative density range. Thus, polynomials defined using FE results allow predicting the Gyroid's homogenized modulus E^* based on the solid material

stiffness E_s for the investigated relative density range without being limited to one specific base material. A reduction of ≈ 20% can be applied to the FE results to account for practical imperfections. Similarly, the homogenized compressive yield strength $R^*_{p0.2}$ is predictable to a good approximation for the investigated *RD* range based on the solid material's compressive yield strength $R_{p0.2,s}$. The analysis of normalized local stresses and plastic strains at the cellular level reveals negligible differences between the investigated base materials and underlines the material-independent characteristic of Gyroid sheet networks at the upper end of their elastic regime.

At relative densities between 10% and ≈ 20%, the solid material's $R_{p0.2,s}$ also provides a sufficient basis to predict the Gyroid's homogenized compressive strength σ^*_{max} with reasonable accuracy. Compared to FEA, the experiments reveal a reduction of ≈ 15%. With increasing relative density, material-dependent plasticity that is not reflected by $R_{p0.2,s}$ dominates σ^*_{max}. To improve the prediction of σ^*_{max}, the authors suggest developing an alternative quantity for the base material strength that incorporates plasticity and ductility. One possibility that will be addressed in upcoming studies is to correlate homogenized plastic strains with equivalent local plastic strains in the Gyroid lattice to find a representative base material stress state for normalization.

Although the present predictive mechanical models have only been validated for Ti6Al4V and Nylon 11, their applicability to other engineering materials is expected, given the substantial differences in the material characteristics of the two investigated materials. Further validation is required to substantiate this broader applicability.

The results of this study enable the design and optimization of Gyroid core structures for compressive loading. The complete homogenized representation of Gyroid sheet networks in FEA, however, requires considering the nonlinear mechanical behavior under compression, tension, and shear. Future studies should extend the methods described in this work to tensile and shear loading conditions. Formulated as a function of the base material properties and *RD*, this approach would allow rapid optimization of the Gyroid core structure under multi-axial loads while keeping computational cost at a minimum.

ORCID iDs

Henri Kammler https://orcid.org/0009-0007-9477-5112
Jan Kube https://orcid.org/0009-0004-4123-242X
Hendrik Traub https://orcid.org/0000-0002-7814-0981
Christian Hühne https://orcid.org/0000-0002-2218-1223

Author contributions

Henri Kammler (first author): Conceptualization, Methodology, Software, Validation, Formal Analysis, Investigation, Data Curation, Writing: Original Draft, Review & Editing, Visualization.
Jan Kube: Conceptualization, Validation, Writing: Review & Editing.
Hendrik Traub: Conceptualization, Validation, Writing: Review & Editing.
Christian Hühne: Funding Acquisition, Project Administration, Resources, Supervision, Writing: Review & Editing.

Funding

The author(s) disclosed receipt of the following financial support for the research, authorship, and/or publication of this article: This research was funded by the Deutsche Forschungsgemeinschaft (DFG, German Research Foundation) under Germany's Excellence Strategy – EXC 2163/1-Sustainable and Energy Efficient Aviation – Project-ID 390881007.

Declaration of conflicting interest

The authors declared no potential conflicts of interest with respect to the research, authorship, and/or publication of this article.

Data availability

Data will be made available by the authors upon request.

References

1. Traub H. *Triply Periodic Minimal Surface Structures for Laminar Flow Control*. Springer Nature Switzerland and Imprint Springer, Cham, 2026.
2. Al-Ketan O and Al-Rub RKA. Multifunctional mechanical metamaterials based on triply periodic minimal surface lattices. *Adv Eng Mater* 2019; 21: 1900524.
3. Chen W, Tang X, Chu X, et al. Impact of catalyst carrier with TPMS structures on hydrogen production by methanol reforming. *Int J Hydrogen Energy* 2024; 58: 1177–1189.
4. Iwaniszyn M, Sindera K, Maszybrocka J, et al. 3D-printed triply periodic minimal surface (TPMS) structures as catalyst carriers. *Chem Eng Res Design* 2024; 209: 37–51.
5. Melchels FPW, Barradas AMC, van Blitterswijk CA, et al. Effects of the architecture of tissue engineering scaffolds on cell seeding and culturing. *Acta Biomater* 2010; 6: 4208–4217.
6. Yeranee K and Rao Y. A review of recent investigations on flow and heat transfer enhancement in cooling channels embedded with triply periodic minimal surfaces (TPMS). *Energies* 2022; 15: 8994.
7. Traub H, Wolff J, Jose S, et al. Concept and design of extended hybrid laminar flow control suction panels. *Sci Rep* 2021. DOI: 10.21203/rs.3.rs-924184/v1.
8. Traub H, Kube J, Jose S, et al. Structural and aerodynamic characteristics of micro-perforated porous sheets for laminar flow control. In: *ASME 2024 aerospace structures, structural dynamics, and materials conference*. 2024, S. 10. DOI: 10.1115/SSDM2024-121620.
9. Kube J, von Soldenhoff R, Thamm K, et al. 3D-gedruckte absaugpaneele für xHLFC-Anwendungen - design und windkanalversuch. In: *DLRK 2024*, 2024.
10. Fohlmeister L, Kube J, Helm S, et al. Wind tunnel measurements of a swept-wing with active suction. In: *AIAA SCITECH 2026 Forum*, 2026. DOI: 10.2514/6.2026-0692.
11. Kube J, Fohlmeister L, Radespiel R, et al. Functionally graded TPMS structures for boundary layer suction on a swept wing. In: *CEAS - AIDAA conference 2025*, 2026, pp.1310–1313. DOI: 10.21741/9781644904251-227.
12. Traub H, Sprengholz M, Teufel D, et al. Structural-mechanical characterisation of triply periodic minimal surface sheet networks: simulation and experiment. In: *AIAA SCITECH 2023 Forum*, 2023. DOI: 10.2514/6.2023-2076.
13. Kammler H, Kube J, Traub H, et al. Validation of material-invariant mechanical models for triply periodic minimal surface structures. *Results Mater* 2026; 29: 100837.

14. Kammler H and Hühne C. Untersuchung der nichtlinearen mechanischen Eigenschaften von Gyroidstrukturen. 2025. In: *DLRK 2025*, 2025.
15. Schöneich J, Kube J, Traub H, et al. Numerical approximation of the flexural properties for additively manufactured sandwich panels with a sheet-based TPMS core. *Result Eng* 2026; 30: 110717.
16. Bauer J, Meza LR, Schaedler TA, et al. Nanolattices: An emerging class of mechanical metamaterials. *Adv Mater* 2017; 29: 1701850.
17. Al-Ketan O, Rowshan R, Palazotto AN, et al. On mechanical properties of cellular steel solids with shell-like periodic architectures fabricated by selective laser sintering. *J Eng Mater Technol* 2019; 141: 021009.
18. Al-Ketan O, Rowshan R and Abu Al-Rub RK. Topology-mechanical property relationship of 3D printed strut, skeletal, and sheet based periodic metallic cellular materials. *Addit Manufact* 2018; 19: 167–183.
19. Abou-Ali AM, Al-Ketan O, Lee D, et al. Mechanical behavior of polymeric selective laser sintered ligament and sheet based lattices of triply periodic minimal surface architectures. *Mater Des* 2020; 196: 109100.
20. Kladovasilakis N, Tsongas K, Kostavelis I, et al. Effective mechanical properties of additive manufactured triply periodic minimal surfaces: experimental and finite element study. *Int J Adv Manufact Technol* 2022; 121: 7169–7189.
21. Zhang L, Feih S, Daynes S, et al. Energy absorption characteristics of metallic triply periodic minimal surface sheet structures under compressive loading. *Addit Manufact* 2018; 23: 505–515.
22. Luo Z, Tang Q, Feng Q, et al. Finite element analysis of the mechanical properties of sheet- and skeleton-gyroid ti6Al4V structures produced by laser powder bed fusion. *Thin-Walled Struct* 2023; 192: 111098.
23. Jin M, Feng Q, Fan X, et al. Investigation on the mechanical properties of TPMS porous structures fabricated by laser powder bed fusion. *J Manuf Process* 2022; 76: 559–574.
24. Sun Q, Sun J, Guo K, et al. Compressive mechanical properties and energy absorption characteristics of SLM fabricated ti6Al4V triply periodic minimal surface cellular structures. *Mech Mater* 2022; 166: 104241.
25. Ciula A, Rubino G and Fanelli P. The mechanical characterization of a gyroid-based metamaterial by compression testing. *Eng Proc* 2025; 85: 17.
26. Shen M, Qin W, Xing B, et al. Mechanical properties of 3D printed ceramic cellular materials with triply periodic minimal surface architectures. *J Eur Ceram Soc* 2021; 41: 1481–1489.
27. Feng G, Li S, Xiao L, et al. Mechanical properties and deformation behavior of functionally graded TPMS structures under static and dynamic loading. *Int J Impact Eng* 2023; 176: 104554.
28. Wang A, Ni X, He D, et al. Compression behavior and energy absorption of TPMS structures prepared by laser powder bed fusion. *Metall Mater Trans B* 2025; 56: 4372–4380.
29. Liang Y, Zhou W, Liu Y, et al. Energy absorption and deformation behavior of 3D printed triply periodic minimal surface stainless steel cellular structures under compression. *Steel Res Int* 2021; 92: 2000411.
30. Ye X, Miao X, Shi X, et al. Effect of porosity and gradient parameters on compressive mechanical properties of sheet gyroid gradient porous structures and construction of mechanical properties prediction model. *Adv Eng Mater* 2024; 26: 2401426.
31. ASTM D20 Committee Standard test method for compressive properties of rigid cellular plastics D1621-16. ASTM International. 2016. DOI: 10.1520/D1621-16.
32. ASTM E28 Committee Test methods of compression testing of metallic materials at room temperature, E9. ASTM International. DOI: 10.1520/E0009-19R25E01.
33. Gibson LJ and Ashby MF. *Cellular solids: Structure and properties*. Cambridge Univ. Press, Cambridge, 1997.
34. Abueidda DW, Bakir M, Abu Al-Rub RK, et al. Mechanical properties of 3D printed polymeric cellular materials with triply periodic minimal surface architectures. *Mater Des* 2017; 122: 255–267.
35. von Schnering HG and Nesper R. Nodal surfaces of Fourier series: Fundamental invariants of structured matter. *Zeitschrift für Phys B Condens Matter* 1991; 83: 407–412.
36. ASTM D20 Committee Standard test method for compressive properties of rigid plastics D695-15. ASTM International. 2015. DOI: 10.1520/D0695-15.
37. DIN 50106:2023-02, Prüfung metallischer Werkstoffe_-Druckversuch bei Raumtemperatur. DIN Media GmbH. DOI: 10.31030/3393741.
38. DIN 50134:2024-07, Prüfung von metallischen Werkstoffen_-Druckversuch an metallischen zellularen Werkstoffen. DIN Media GmbH. DOI: 10.31030/3533999.
39. Harte Schaumstoffe – Bestimmung der Druckeigenschaften (ISO 844:2021). 2021.
40. Simsek U, Akbulut A, Gayir CE, et al. Modal characterization of additively manufactured TPMS structures: comparison between different modeling methods. *Int J Adv Manufact Technol* 2021; 115: 657–674.
41. Tevet O, Svetlizky D, Harel D, et al. Measurement of the anisotropic dynamic elastic constants of additive manufactured and wrought ti6Al4V alloys. *Materials* 2022; 15: 638.
42. Lammens N, Kersemans M, de Baere I, et al. On the visco-elasto-plastic response of additively manufactured polyamide-12 (PA-12) through selective laser sintering. *Polym Test* 2017; 57: 149–155.
43. DIN Deutsches Institut für Normung e. V. DIN EN ISO 604:2003-12 Kunststoffe - bestimmung von druckeigenschaften (ISO 604:2002): Norm. 2003.